A Non-iterative Reconstruction Algorithm for Single Pixel Spectral Imaging with Side Information

Jorge Bacca*, Claudia V. Correa†, and Henry Arguello‡
Department of Computer Science, Universidad Industrial de Santander
Email: *jorge.bacca1@correo.uis.edu.co, †clavicop@uis.edu.co, ‡henarfu@uis.edu.co

***Abstract*—Compressive spectral imaging (CSI) allows the acquisition of spatial information of a scene along multiple spectral bands using fewer projected measurements than traditional scanning methods. In general, to obtain high resolution spatial and spectral information, expensive detectors and sophisticated optical devices are required. Fortunately, the single-pixel camera (SPC) is a low-cost optical architecture since it uses a light sensor compared to CSI architectures with larger sensors. However, this advantage is overshadowed by the large number of projections needed to recover the spectral image, which entails large acquisition times. Alternatively, high-resolution spectral images can be obtained using SPC with side-information, without significantly increasing acquisition costs. However, this approach retrieves improved resolution images applying iterative and computationally expensive algorithms. This paper proposes a non-iterative method that combines the spectral information of SPC and the side information of a multispectral image to recover high resolution spatial and spectral information. The proposed fast compressive spectral imaging (FCSI) reconstruction method exploits the fact that the spatial-spectral data lie in a low dimensional subspace. This methodology allows to reduce the number of required measurements in the SPC as well as the computation time of the reconstruction. Simulations and experimental results show the effectiveness of the proposed method compared to similar approaches, both in reconstruction quality and sample complexity.**

I. Introduction

Spectral imaging systems sense two-dimensional (2D) spatial information (x, y) of a scene along the electromagnetic spectrum (λ). These images provide richer spectral information of the scene compared to RGB color images, which enables material and object identification in different applications such as biomedical imaging [1], crop identification [2] and surveillance [3]. Traditionally, scanning-based devices such as whiskbroom and pushbroom spectrometers are used to measure the spectrum at all spatial points of the scene [4]. However, some applications require high-resolution images; therefore, hundreds or thousands of spectral bands need to be sensed, which makes spectral data cube acquisition and processing a challenging problem under these setups.

Alternatively, compressive spectral imaging (CSI) acquires compressed projections of the entire data cube instead of direct measurements of all voxels [5]. CSI allows to reduce the dimensionality of the data without further processing steps. Moreover, to obtain the spectral image from the compressed projections, numerical optimization methods based on sparse priors are used [5]. From an implementation point of view, CSI architectures employ optical elements such as coded apertures, spatial light modulators, prisms, gratings and intensity detectors, to obtain the projected measurements [6]. However, high-resolution image acquisition requires sophisticated optical devices such as specialized prisms or large detectors that enable a detailed discretization of the spectrum but considerably increase the implementation costs [6]. Therefore, achieving high-resolution spectral images at lower implementation costs is still an open problem.

The single-pixel camera (SPC) is a low-cost CSI architecture, since it uses a single spatial pixel as sensor to acquire the entire image, compared with other CSI devices which use large and more expensive 2D detectors [6]. Nonetheless, the robustness of this architecture is overshadowed by the large number of projections needed to obtain good quality reconstructions [6]. Alternatively, dual arm optical systems have been proposed to capture both SPC measurements and an auxiliary multispectral image such that fewer projections are acquired [7], [8]. More specifically, one arm of these systems captures SPC measurements, while the other arm acquires an RGB or panchromatic image of the scene that is later used to guide the reconstruction process. This approach exploits the high spectral resolution of the SPC and the high spatial resolution of the side information to obtain high-quality images from few measurements, which in turn, reduces acquisition times. Reconstructions, however, are still expensive due to the iterative nature of employed algorithms.

This work proposes a non-iterative reconstruction algorithm for single pixel spectral imaging using a multispectral image as side information. This method exploits the natural characteristics of spectral images, that are assumed to lie in a low dimensional subspace [9], unlike the sparse representations in [7], [8]. This characteristic allows spectral images to be treated as low-rank structures, such that in the absence of noise, the algorithm can exactly calculate a basis for the subspace and image coefficients, when the number of measurements in the SPC and the number of bands in the multispectral image are larger than the dimension of the subspace. This methodology allows to reduce the number of measurements in the SPC as well as the computation time of the reconstruction. Specifically, the proposed algorithm is up to 200 times faster since it does not perform iterations and, improves reconstruction quality in up to 10 dB of peak signal- to-noise ratio (PSNR) for a noise level of 30 dB of SNR compared with state-of-the-art iterative reconstruction algorithms based on side information.

Throughout the paper, we denote each voxel of a $M \times N \times L$ hyperspectral image as $f_{(i,j,l)}$ where $i = 1, \ldots, M$, $j = 1, \ldots, N$ index the spatial coordinates and $l = 1 \ldots, L$ represents the spectral band index.

This work was partially funded by the Regional Program STIC-AmSud and Colciencias through the project with code 309-2018. C. V. Correa was funded by UIS through the VIE program for postdoctoral researchers.

978-9-0827-9703-9/19/$31.00 ©2019 IEEE

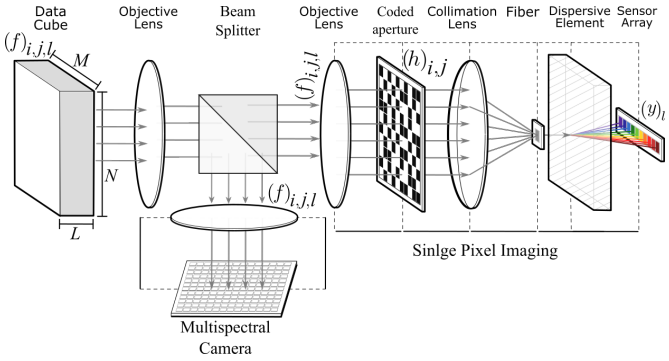

Fig. 1. Single Pixel Imaging optical flow used to acquire high-resolution image with multispectral camera as side information.

II. Forward Sensing Model of the Single Pixel Camera with Side Information

The setup of the single pixel camera for spectral imaging is shown in Figure 1 [10], [11]. This architecture comprises a coded aperture that spatially encodes the scene and, it is mathematically modeled as a binary function $h_{(i,j)} \in \{-1, 1\}$. Then, the encoded scene is projected into a single spatial point by a collimation lens, where a whiskbroom spectrometer is used as a detector, which splits the scene into its spectral bands. This system can be modeled as a linear mapping, where all pixels (i, j) of the image $f_{(i,j,l)}$ in the l-th band are projected to a single point $y_{(l)}$ as

$$y_{(l)} = \sum_{i=1}^{M} \sum_{j=1}^{N} h_{(i,j)} f_{(i,j,l)}. \tag{1}$$

In order to obtain different projections of the same scene, the configuration of the coded aperture is changed such that multiple shots are acquired. Assuming K shots, Eq. (1) can be expressed as a linear system of the form

$$\mathbf{Y} = \mathbf{H}\mathbf{F}, \tag{2}$$

where $\mathbf{H} \in \{-1, 1\}^{K \times MN}$ denotes the SPC sensing matrix, in which the k-th row is the vectorization of the coded aperture used for that particular shot; $\mathbf{Y} \in \mathbb{R}^{K \times L}$ represents the observation matrix, and $\mathbf{F} \in \mathbb{R}^{MN \times L}$ is the hyperspectral data cube organized as $\mathbf{F} = [\mathbf{f}_{(1)}, \ldots, \mathbf{f}_{(MN)}]^T$, where $\mathbf{f}_{(p)} \in \mathbb{R}^L$ represents the spectral signature of the p-th pixel. Figure 1 includes a second arm, in which a multispectral image of the same scene is captured. It is generally assumed that the observed multispectral images are obtained under the same atmospheric and illumination conditions; thus, these observations result from linear spectral degradations of the full resolution image $\mathbf{F}$. Given that the number of bins, i.e. spectral bands, measured by the spectrometer is $L' < L$, this work assumes that each channel of $\mathbf{F}$ matches the range spanned by Δ spectrometer bins such that

$$f_{M(i,j,l)} = \sum_{k=(l-1)\Delta+1}^{l\Delta} \omega_{(k)} f_{(i,j,k)}, \tag{3}$$

where f_M represents the multispectral image and $\omega_{(k)}$ denotes the spectral response of the multispectral sensor. Equation (3) can be expressed in matrix form as

$$\mathbf{F}_M = \mathbf{F}\mathbf{D}, \tag{4}$$

where $\mathbf{D}$ is a down-sampling matrix accounting for the decimation and the spectral response of the sensor, with a factor of Δ given the gap between the spectrometer and the resolution of the multispectral image.

Traditional models to recover the hyperspectral image from the set of SPC measurements in (2) and the side information from (3), use a vectorization form of the problem [7]. Letting $\tilde{\mathbf{f}} \in \mathbb{R}^{MNL}$ be the vectorized image of the form $\tilde{\mathbf{f}} = [\mathbf{f}_{(1)}^T, \cdots, \mathbf{f}_{(MN)}^T]^T$ [7], assume a sparse prior such that the image can be written as a linear combination of S elements on a basis $\mathbf{\Psi}$, i.e. $\tilde{\mathbf{f}} = \mathbf{\Psi}\boldsymbol{\theta}$ with $S << MNL$. Therefore, the optimization problem for the reconstruction model is expressed as

$$\hat{\mathbf{f}} = \mathbf{\Psi} \left\{ \arg\min_{\boldsymbol{\theta}} \|\tilde{\mathbf{H}}\mathbf{\Psi}\boldsymbol{\theta} - \tilde{\mathbf{y}}\|_2^2 + \|\tilde{\mathbf{D}}\mathbf{\Psi}\boldsymbol{\theta} - \mathbf{f}_m\|_2^2 + \tau\|\boldsymbol{\theta}\|_1 \right\}, \tag{5}$$

where $\tilde{\mathbf{H}}$ is the vector representation of $\mathbf{H}$ in (2), expressed as $\tilde{\mathbf{H}} = \mathbf{I}_L \otimes \mathbf{H}$ with $\otimes$ as the Kronecker product, and $\mathbf{I}_L$ is a $L \times L$ identity matrix; $\tilde{\mathbf{y}}$ and $\mathbf{f}_m$ represent the vectorization of the matrix of projections $\mathbf{Y}$ and the multispectral image $\mathbf{F}_M$, in (2) and (3), respectively. Finally, define $\mathbf{R} \in \mathbb{R}^{1 \times \Delta}$ as the spectral response of the multispectral sensor and $\tilde{\mathbf{D}} = \mathbf{I}_L \otimes (\mathbf{R} \otimes \mathbf{I}_{MN})$ represents the down-sampling operator. The ℓ_1-norm term promotes sparsity and τ is a regularization parameter for the sparsity and noise trade-off.

III. Non-iterative Reconstruction Algorithm

Unlike the problem in (5) that uses the sparse representation of the spectral image, this work proposes to exploit the fact that the data lies in a $C-$dimensional subspace $\mathcal{S}$, with $C << L$. This is a common approach used in many applications [12], [13], [14], where each spectral vector $\mathbf{f}_{(p)}$ is expressed (non-uniquely[1]) as

$$\mathbf{f}_{(p)} = \mathbf{E}\mathbf{a}_{(p)}, \ for\ p = 1, \cdots MN, \ \ and \ \ \mathbf{F} = \mathbf{A}\mathbf{E}, \tag{6}$$

with $\mathbf{A} = [\mathbf{a}_{(1)} \cdots \mathbf{a}_{(MN)}]$, where $\mathbf{a}_{(p)} \in \mathbb{R}^C$ are the representation coefficients of $\mathbf{f}_{(p)}$ with respect to $\mathbf{E}$, whose columns form a basis for the subspace. Notice that this formulation can be applied to the linear mixture model (LMM), where the matrix $\mathbf{E}$ may be interpretable as the endmembers matrix, and $\mathbf{A}$ as the corresponding abundance matrix. However, this work focuses on the general case of a blind reconstruction of $\mathbf{A}$ and $\mathbf{E}$. Note that, from (4) we have that the multispectral image maintains the spatial sizes of the scene, however, the spectral dimension exhibits a degradation of the form

$$\mathbf{F}_M = \mathbf{A}\mathbf{E}\mathbf{D} = \mathbf{A}\tilde{\mathbf{E}}, \tag{7}$$

where $\tilde{\mathbf{E}} = \mathbf{E}\mathbf{D}$ is the decimation basis. Notice that in the LMM framework, the decimation matrix $\tilde{\mathbf{E}}$ can be obtained using some endmember extraction algorithm such as Vertex complex analysis (VCA) [14] with C as input, or any other way to find the basis of a subspace such as the truncated SVD decomposition [15]. Since $\tilde{\mathbf{E}}$ is a base of the subspace $\mathcal{S}$, its rows are linearly independent; therefore, the abundance matrix can be recovered as

$$\mathbf{A} = \tilde{\mathbf{F}}_M \tilde{\mathbf{E}}^T \left(\tilde{\mathbf{E}} \tilde{\mathbf{E}}^T \right)^{-1}. \tag{8}$$

[1]The matrix $\mathbf{F}$ can be rewritten as $\mathbf{F}^T = (\mathbf{A}\mathbf{R})(\mathbf{R}^T\mathbf{E})$ for any rotation matrix $\mathbf{R}$.

On the other hand, notice that the SPC in (1) can be expanded as

$$y_{(l)} = \sum_{i=1}^{M}\sum_{j=1}^{N} h_{(i,j)} \sum_{c=1}^{C} e_{(c,l)} a_{(i,j,c)} = \sum_{c=1}^{C} e_{(c,l)} \sum_{i=1}^{M}\sum_{j=1}^{N} h_{(i,j)} a_{(i,j,c)}, \quad (9)$$

yielding an interesting observation: in this architecture, the codification only affects the abundance map. Hence, for all shots, (9) can be expressed in matrix form as

$$\mathbf{Y} = \mathbf{HAE}, \quad (10)$$

and since $\mathbf{A}$ is obtained from (8), the reconstruction of $\mathbf{E}$, assuming that the product of $\mathbf{HA}$ is full column rank, can be obtained as

$$\mathbf{E} = \left(\mathbf{A}^T\mathbf{H}^T\mathbf{HA}\right)^{-1}\mathbf{A}^T\mathbf{H}^T\mathbf{Y}. \quad (11)$$

Using $\mathbf{A}$ from (8) and $\mathbf{E}$ from (11), $\mathbf{F}$ can be recovered as in (6) ($\mathbf{F} = \mathbf{AE}$). Algorithm 1 summarizes the steps of the proposed method. Notice that exact reconstruction of $\mathbf{F}$, in the absence of noise, can be achieved under the conditions established in Theorem III.1, which depends on the number of shots and the decimation factor Δ.

Algorithm 1 Non-iterative hyperspectral image reconstruction

1: Measurements $\mathbf{Y}$, Multispectral image $\mathbf{F}_M$, sensing matrix
2: $\mathbf{H}$, and dimension of the subspace C.
3: $\tilde{\mathbf{E}} \leftarrow$VCA$(\mathbf{F}_M^T, C)$
4: $\mathbf{A} \leftarrow \tilde{\mathbf{F}}_M\tilde{\mathbf{E}}^T\left(\tilde{\mathbf{E}}\tilde{\mathbf{E}}^T\right)^{-1}$
5: $\mathbf{E} = \left(\mathbf{A}^T\mathbf{H}^T\mathbf{HA}\right)^{-1}\mathbf{A}^T\mathbf{H}^T\mathbf{Y}$
6: $\mathbf{F}$= $\mathbf{AE}$
7: The hyperspectral image $\mathbf{F}$

Theorem III.1. Noiseless exact reconstruction: Assume that a spectral image $\mathbf{F} \in \mathbb{R}^{L\times MN}$ has rank $C \leq \min\{L, MN\}$, such that it can be factorized as $\mathbf{F} = \mathbf{AE}$, where $\mathbf{E} \in \mathbb{R}^{L\times C}$ and $\mathbf{A} \in \mathbb{R}^{C\times MN}$. Also, consider that $K \geq C$ shots are taken in the SPC, with the measurement matrix $\mathbf{H} \in \mathbb{R}^{K\times MN}$, independently drawn at random from a Rademacher distribution. Then, $\mathbf{F}$ can be exactly recovered from the compressed measurements $\mathbf{Y}$ by recovering $\mathbf{A}$ and $\mathbf{E}$ from the solution of (8) and (11), respectively, if a multispectral image of the scene with $C \leq \frac{L}{\Delta}$ is obtained as side information.

Proof: The proof of Theorem III.1 is in Appendix A. ■

IV. Simulations and Results

In this section, the performance of the proposed method is evaluated using simulated and real data. The results shown are the average of 10 trial runs using random coded apertures with {-1,1} entries. All simulations were implemented in Matlab 2017a on an Intel Core i7 3.41Ghz CPU with 32 GB RAM.

A. Test 1: Performance of the proposed method

The first experiment demonstrates the exact recovery of the non-iterative algorithm when the conditions of Theorem III.1 are guaranteed. For this, the Jasper dataset of size $128 \times 128 \times 198$, which contains $C = 4$ endmembers (Tree, Water, Dirt and Road) was used [16]. Figure 2 shows the exact reconstruction of endmembers and abundance maps obtained with the proposed method in the limit case $L' = K = 4$ given in Theorem III.1. It can be seen that large peak-signal-to-noise (PSNR) values are obtained for the abundance maps and estimated endmembers exhibit a very low normalized mean-squared error (NMSE). Notice that, Theorem III.1 guarantees exact reconstruction in the absence of noise when, for this data set, $L' \geq 4$ and $K \geq 4$. However, it does not guarantee accuracy for noisy measurements. For this reason, simulations are performed to evaluate the reconstruction quality varying the compression ratio in the SPC and the number of bands L' in the multispectral image for noisy scenarios. The compression ratio for SPC is defined as

$$\gamma = \frac{K}{MN}. \quad (12)$$

In addition, zero-mean Gaussian noise with 20 and 40 SNR defined as $\text{SNR} = 10\log_{10}\frac{\|\mathbf{Y}\|_F^2}{\mathbb{E}\|\mathbf{N}\|_F^2}$ was added to the compressive measurements in (2) and the multispectral image (4), where $\mathbb{E}$ denotes the expected value and $\mathbf{N}$ is the additive noise. Figure 3 shows the quality of the reconstructions measured in PSNR, for different compression ratios γ and different number of spectral bands L', i.e. $L' = 1$ denotes a panchromatic image and $L' = 3$ is an RGB image. Note that, as the number of bands in the multispectral image increases, the quality of the reconstruction using the proposed algorithm improves significantly. Otherwise, when the compression ratio increases in the SPC, the quality does not increase significantly, but it at least requires a compression ratio of $\gamma = 0.01$ to show a stable behavior.

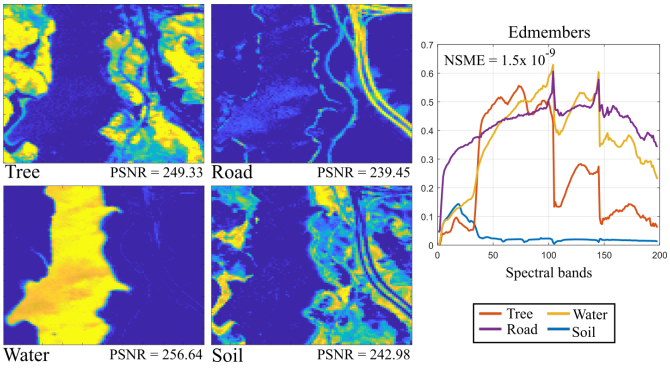

Fig. 2. Endmembers and abundance maps reconstruction in absence of noise with the limit case $L' = K = 4$ for Jasper Dataset

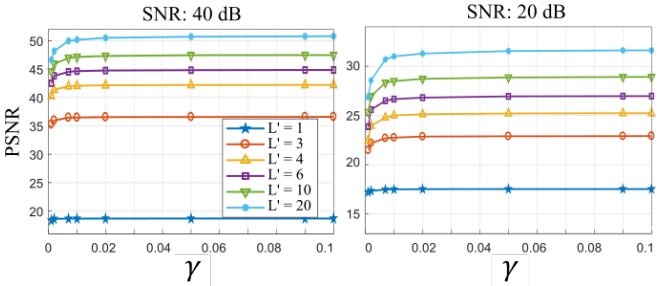

Fig. 3. Reconstruction quality measured in PSNR for different levels of compression and number of bands in the multispectral image (L') for noisy measurements (left) 40 dB and (right) 20 dB of SNR.

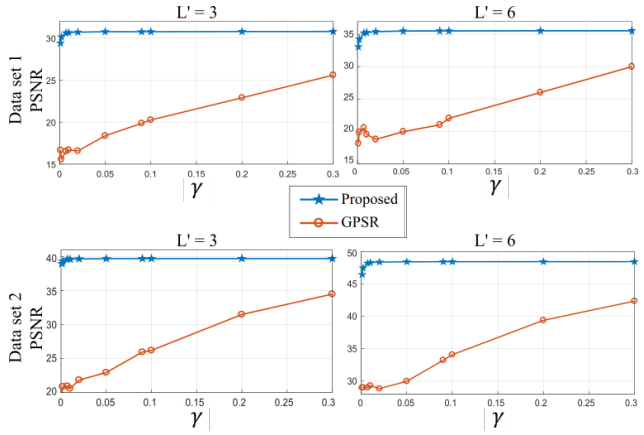

Fig. 4. Reconstruction quality as a function of the compression ratio γ for $L' = 3$ and $L' = 6$, for two different data sets.

B. Test 2: Comparison with iterative reconstruction methods

The Jasper image and an additional data cube of 256×256 pixels of spatial resolution and 30 spectral bands [17], were used in this test. Unlike Jasper, this data set does not have a defined rank; therefore, the noise considered in the experiment is caused by imposing a low rank constraint in the proposed method. The results are is compared with those obtained by solving (5) using the Gradient Projection for Sparse Reconstruction (GPSR) algorithm [18], for a basis representation $\mathbf{\Psi} = \mathbf{\Psi}_1 \otimes \mathbf{\Psi}_{2D}$, where $\mathbf{\Psi}_1$ is a 1D discrete cosine transform, and $\mathbf{\Psi}_{2D}$ is a 2D wavelet Symmlet 8 basis [7]. The regularization parameter τ in (5) was determined using a cross-validation strategy for each data set and different compression ratios. It is worth noting that the proposed method does not require this tunable parameter; it only needs the parameter C that is related to the number of measurements, which is an advantage in implementation details.

Figure 4 shows the average reconstruction quality of the proposed method, measured in PSNR, compared with GPSR solving (5), using 3-band (RGB) and 6 bands as side information. Additionally, the compression rate was varied up to 0.3, i.e. with a 30% of compressed measurements,

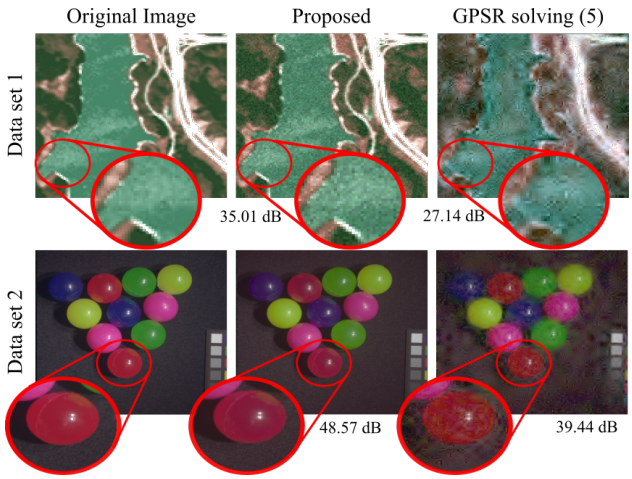

Fig. 5. Visual reconstruction comparison for $L' = 6$ and $\gamma = 0.1$ with two data sets.

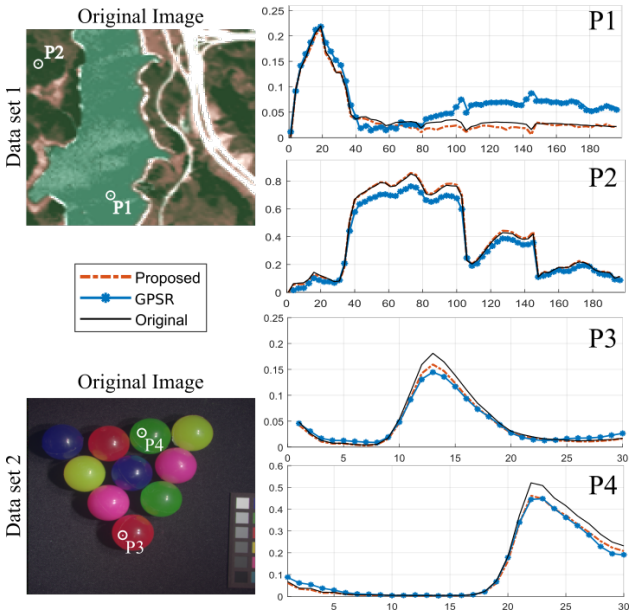

Fig. 6. Spectral signatures of P1, P2, P3 and P4 of the two data set compared with the reconstructed spectral points.

for both data sets. For this test, the measurements of data set 1 (Jasper image) were contaminated with 30dB SNR Gaussian noise. Notice that the proposed non-iterative method outperforms the traditional side information method in up to 10 dB. Additionally, the quality of the reconstruction in GPSR algorithm increases as more shots are taken, in contrast with the proposed method. This is based on the fact that the proposed method is a non-iterative algorithm and provides similar accuracy if the condition presented in Theorem III.1 is satisfied.

Additionally, Figure 5 shows the visual reconstruction using an RGB mapping of the images, for $L' = 6$ and $\gamma = 0.2$. Notice that the proposed method provides more detailed images as shown in the zoomed portions. Furthermore, Figure 6 compares two spectral points per data set, for the proposed and GPSR methods. It can be seen that the spectral signatures obtained by the proposed method are closer to the original.

Moreover, Table I compares the reconstruction time of the proposed method compared to GPSR solving (5) for the same configuration used in the previous test with 150 iterations

TABLE I. RECONSTRUCTION TIME FOR DIFFERENT DATA SETS AND COMPRESSION RATIOS.

	Reconstruction Time [s]							
	Proposed Method				**GPSR solving (5)**			
γ	**Data set 1**		**Data set 2**		**Data set 1**		**Data set 2**	
	L'=3	L'=6	L'=3	L'=6	L'=3	L'=6	L'=3	L'=6
0.001	**0.07**	**0.07**	**0.02**	**0.03**	106.32	107.65	16.24	16.37
0.002	**0.07**	**0.09**	**0.02**	**0.03**	109.44	111.456	17.72	17.07
0.007	**0.08**	**0.08**	**0.02**	**0.03**	143.57	154.23	22.77	22.49
0.01	**0.08**	**0.08**	**0.02**	**0.04**	158.69	168.41	25.03	24.69
0.02	**0.10**	**0.10**	**0.02**	**0.04**	225.22	256.42	34.16	34.45
0.05	**0.14**	**0.14**	**0.05**	**0.06**	420.66	455.17	62.42	64.01
0.09	**0.19**	**0.21**	**0.07**	**0.09**	646.35	660.41	97.19	101.70
0.10	**0.21**	**0.22**	**0.08**	**0.09**	761.42	774.91	107.74	106.12
0.20	**0.35**	**0.35**	**0.14**	**0.15**	1270.05	1304.48	191.25	188.89
0.30	**0.47**	**0.48**	**0.20**	**0.21**	1727.65	1799.94	280.32	268.08

(which is the number of iterations needed to obtain good reconstructions in the conventional method). The best time for each case is shown in boldface. It can be seen that the proposed method is significantly faster in comparison with the iterative algorithm, specifically, it is up to 200 times faster than GPSR.

V. Conclusion

A non-iterative algorithm for reconstructing high-resolution spectral images for single pixel imaging with a multispectral camera as side information has been proposed. The proposed method enables exact reconstruction in the absence of noise when the number of measurements for the SPC and the number of bands in the multispectral image is larger than the subspace dimensionality of the data. Moreover, simulations show that the proposed method also performs well with noisy measurements. Specifically, the proposed algorithm is up to 200 times faster and overcomes reconstruction algorithms based on side information. In particular, a gain of up to 10 dB in image reconstruction quality for a level noise of 30 dB of SNR was obtained with respect to the GPSR algorithm.

Appendix A
Proof of Theorem I

Proof: Given the single pixel measurements $\mathbf{Y} = \mathbf{HF}$ and the multispectral image $\mathbf{F}_M = \mathbf{FD}$ as side information, where $\mathbf{F} \in \mathbb{R}^{MN\times L}$ has rank $C \leq \min\{L, MN\}$. $\mathbf{F}$ can be factorized as $\mathbf{F} = \mathbf{AE}$, where $\mathbf{E} \in \mathbb{R}^{C\times L}$ is a full row rank matrix, and $\mathbf{A} \in \mathbb{R}^{MN\times C}$ is a full column rank matrix. Then, with the structure of the decimation matrix shown in (3), we have that

$$\mathbf{F}_M = \mathbf{AED}, \tag{13}$$

where $\mathbf{D} \in \mathbb{R}^{L\times \frac{L}{\Delta}}$, since $C \leq \frac{L}{\Delta}$. The rank of the multispectral image in (13) is

$$\text{rank}(\mathbf{F}_M) = \text{rank}(\mathbf{FD}) = \text{rank}(\mathbf{F}). \tag{14}$$

Therefore, it can be factorized as $\mathbf{F}_M = \mathbf{A}\tilde{\mathbf{E}}$, where $\tilde{\mathbf{E}} = \mathbf{ED}$ is a full row rank matrix, which can be obtained following the lines 3-4 in Algorithm 1. Consequently, the matrix $\mathbf{A}$ can be obtained as in (8) since the rows of $\tilde{\mathbf{E}}$ are linearly independent, and $\tilde{\mathbf{E}}\tilde{\mathbf{E}}^T$ is invertible.

After obtaining $\mathbf{A}$, $\mathbf{E}$ can be recovered using (11). It is necessary to show that the matrix $\mathbf{HA}$ is full column rank. Since $\mathbf{H} \in \{-1, 1\}^{K\times MN}$ is drawn from a Rademacher distribution, its rows are general linear positions with probability one [19]. Additionally, as $K > C$, the sensing matrix $\mathbf{Y}$ spans the range of $\mathbf{F}$, almost sure. Therefore, (10) can be written as

$$\mathbf{Y} = \mathbf{HAE}, \tag{15}$$

where $\mathbf{A}$ is already known because it was calculated in a previous step. Since the rank of the product of two full rank matrices is the minimum rank matrix, we have that $\mathbf{HA}$ is full column rank, therefore, the matrix $\mathbf{E}$ can be calculated as in (11). Thus, the result holds. ■

References

[1] G. Lu and B. Fei, "Medical hyperspectral imaging: a review," *Journal of biomedical optics*, vol. 19, no. 1, p. 010901, 2014.

[2] J. Bacca, C. Hinojosa, and H. Arguello, "Kernel sparse subspace clustering with total variation denoising for hyperspectral remote sensing images," in *Mathematics in Imaging*, pp. MTu4C–5, Optical Society of America, 2017.

[3] P. W. Yuen and M. Richardson, "An introduction to hyperspectral imaging and its application for security, surveillance and target acquisition," *The Imaging Science Journal*, vol. 58, no. 5, pp. 241–253, 2010.

[4] Y. Garini, I. T. Young, and G. McNamara, "Spectral imaging: principles and applications," *Cytometry Part A: The Journal of the International Society for Analytical Cytology*, vol. 69, no. 8, pp. 735–747, 2006.

[5] G. R. Arce, D. J. Brady, L. Carin, H. Arguello, and D. S. Kittle, "Compressive coded aperture spectral imaging: An introduction," *IEEE Signal Processing Magazine*, vol. 31, no. 1, pp. 105–115, 2014.

[6] X. Cao, T. Yue, X. Lin, S. Lin, X. Yuan, Q. Dai, L. Carin, and D. J. Brady, "Computational snapshot multispectral cameras: Toward dynamic capture of the spectral world," *IEEE Signal Processing Magazine*, vol. 33, no. 5, pp. 95–108, 2016.

[7] H. Garcia, C. V. Correa, K. Sánchez, E. Vargas, and H. Arguello, "Multi-resolution coded apertures based on side information for single pixel spectral reconstruction," in *2018 26th European Signal Processing Conference (EUSIPCO)*, pp. 2215–2219, IEEE, 2018.

[8] A. Jerez, H. Garcia, and H. Arguello, "Single pixel spectral image fusion with side information from a grayscale sensor," in *2018 IEEE 1st Colombian Conference on Applications in Computational Intelligence (ColCACI)*, pp. 1–6, IEEE, 2018.

[9] J. Bacca, C. V. Correa, and H. Arguello, "Noniterative hyperspectral image reconstruction from compressive fused measurements," *IEEE Journal of Selected Topics in Applied Earth Observations and Remote Sensing*, 2019.

[10] T. Sun and K. Kelly, "Compressive sensing hyperspectral imager," in *Computational Optical Sensing and Imaging*, p. CTuA5, Optical Society of America, 2009.

[11] F. Soldevila, E. Irles, V. Durán, P. Clemente, M. Fernández-Alonso, E. Tajahuerce, and J. Lancis, "Single-pixel polarimetric imaging spectrometer by compressive sensing," *Applied Physics B*, vol. 113, no. 4, pp. 551–558, 2013.

[12] C. Yang, J. H. Everitt, Q. Du, *et al.*, "Applying linear spectral unmixing to airborne hyperspectral imagery for mapping yield variability in grain sorghum and cotton fields," *Journal of Applied Remote Sensing*, vol. 4, no. 041887, p. 041887, 2010.

[13] J. Bacca, H. Vargas, and H. Arguello, "A constrained formulation for compressive spectral image reconstruction using linear mixture models," in *Proc. Conf. CAMSAP*, pp. 1–5, IEEE, 2017.

[14] J. M. P. Nascimento and J. M. B. Dias, "Vertex component analysis: a fast algorithm to unmix hyperspectral data," *IEEE Transactions on Geoscience and Remote Sensing*, vol. 43, pp. 898–910, April 2005.

[15] L. Cattani, D. Maillet, F. Bozzoli, and S. Rainieri, "Estimation of the local convective heat transfer coefficient in pipe flow using a 2d thermal quadrupole model and truncated singular value decomposition," *International Journal of Heat and Mass Transfer*, vol. 91, pp. 1034–1045, 2015.

[16] F. Zhu, Y. Wang, B. Fan, S. Xiang, G. Meng, and C. Pan, "Spectral unmixing via data-guided sparsity," *IEEE Transactions on Image Processing*, vol. 23, no. 12, pp. 5412–5427, 2014.

[17] F. Yasuma, T. Mitsunaga, D. Iso, and S. K. Nayar, "Generalized assorted pixel camera: postcapture control of resolution, dynamic range, and spectrum," *IEEE transactions on image processing*, vol. 19, no. 9, pp. 2241–2253, 2010.

[18] M. A. Figueiredo, R. D. Nowak, and S. J. Wright, "Gradient projection for sparse reconstruction: Application to compressed sensing and other inverse problems," *IEEE Journal of selected topics in signal processing*, vol. 1, no. 4, pp. 586–597, 2007.

[19] G. Martín and J. M. Bioucas-Dias, "Hyperspectral blind reconstruction from random spectral projections," *IEEE Journal of Selected Topics in Applied Earth Observations and Remote Sensing*, vol. 9, no. 6, pp. 2390–2399, 2016.